Peer-reviewed version available at *Colloids Interfaces* **2018**, *2*, 23; doi:10.3390/colloids2020023

Article

Waterflooding of Surfactant and Polymer Solutions in a Porous Media Micromodel

Hsiang-Lan Yeh and Jaime J. Juárez [1,*]

[1] Department of Mechanical Engineering, Iowa State University, 2529 Union Drive, Ames, IA 50011
* Correspondence: jjuarez@iastate.edu; Tel.: +01-515-294-3298

Abstract: In this study, we examine microscale waterflooding in a randomly close-packed porous medium. Three different porosities are prepared in a microfluidic platform and saturated with silicone oil. Optical video fluorescence microscopy is used to track the water front as it flows through the porous packed bed. The degree of water saturation is compared to water containing two different types of chemical modifiers, sodium dodecyl sulfate (SDS) and polyvinylpyrrolidone (PVP), with water in the absence of a surfactant used as a control. Image analysis of our video data yield saturation curves and calculate fractal dimension, which we use to identify how morphology changes the way an invading water phase moves through the porous media. An inverse analysis based on the implicit pressure explicit saturation (IMPES) simulation technique uses mobility ratio as an adjustable parameter to fit our experimental saturation curves. The results from our inverse analysis combined with our image analysis show that this platform can be used to evaluate the effectiveness of surfactants or polymers as additives for enhancing the transport of water through an oil-saturated porous medium.

Keywords: Porous Media; Optical Video Microscopy; Microfluidics; Waterflooding; Surfactants; Polymers

1. Introduction

Understanding multiphase flows in porous media is critical for enhancing the recovery of oil from the porous bedrock [1]. When a reservoir is tapped through a wellbore in the bedrock for the first time, a pressure differential between the reservoir and the wellbore can be used as a primary form of recovery. Once the pressure differential reaches hydrostatic equilibrium, secondary forms of recovery such as waterflooding (i.e., water injection) can used to extract the remaining oil [2]. Approximately 40% of the total available oil is extracted using these two methods.[3]

Chemical methods, including the addition of surfactants, polymers or alkali to the water, are used to enhance the recovery of oil beyond the 40% limit encountered with hydrostatic pressure and water [4]. Surfactants in water reduce the interfacial surface tension between the water and the oil, which also reduce the capillary forces and enhance the oil displacement efficiency [5,6]. Polymers act as viscosifying agents, which reduce the viscosity and density mismatch between the water and oil phases. A reduction in the relative difference between viscosity and density, known as mobility, allows for increased oil displacement [7,8]. A combination of chemical methods are proposed as an effective method for enhancing oil recovery [9].

Understanding how these mechanisms act in isolation to each other and how they can be combined is critical for improving oil displacement efficiency. However, transport through oil-bearing porous media occurs at a rate of 1 linear foot per day [10] and the direct observation of

Peer-reviewed version available at Colloids Interfaces 2018, 2, 23; doi:10.3390/colloids2020023

large-scale oil displacement phenomena can take weeks [11], which makes study of multiphase processes slow and difficult. The slow rate of observation is a direct result of transport through the interconnected network of grains that make up the porous media.[12] Micromodels based on lab-on-a-chip platforms offer one possible approach to experimentally investigating multiphase processes in porous media micromodels at shorter time scales.[13]

Micromodels enable direct observation of flow through porous media. In this approach, an optically transparent flow cell is constructed with a uniform distribution of glass or quartz beads dispersed inside to act as the porous grain structure and direct visualization of the flow is then performed using optical microscopy techniques.[14,15] Although advances in microfabrication technology allow for manufacturing complex pore structures[16–18], most micromodels used to study multiphase fluid flow through pore media have been done in rectangular pore bodies and throats.[19–25] Computer-aid design of microchannels can be used to mimic heterogeneous porous media structure [26,27].

This article presents a microfluidic platform for evaluating chemical methods to enhance oil recover through the waterflooding process. The platform consists of a 750 μm wide microfluidic channel into which glass beads are dispersed in silicone oil and packed to form a random porous bed. Optical fluorescence microscopy is used to track the introduction of an aqueous fluorescent dye to the main channel through a side channel. Tracking the dye enables us to evaluate of the saturation of the aqueous phase relative to the oil phase. The injection of pure water is compared to injection of water containing two different kinds of chemical modifiers, sodium dodecyl sulfate (SDS) and polyvinylpyrrolidone (PVP). SDS is an anionic surfactant and PVP is a polymer. Our analysis based on optically tracking the invasion of the aqueous phase demonstrate that chemical modifiers significantly improve the displacement of oil from the microfluidic channel, although image analysis of fractal dimension morphology illustrate differences in aqueous phase invasion.

Micromodels offer qualitative information on flow characteristics, but quantitative tools for comparison to experiment are not well-developed [28]. To address this gap in quantitative data evaluation, we introduce an inverse analysis based on implicit pressure explicit saturation (IMPES) to determine the mobility of our surfactant and polymer phases. The analysis presented here offers an approach to interpreting two-phase flow data in a porous microfluidic channel and obtaining parameters such as saturation and mobility that can be used to compare effectiveness of different chemical methods for enhancing oil recovery. Optical measurements of waterflooding can also guide the assessment of other multiphase flow problems, such as the transport of sequestered carbon dioxide in porous bedrock [29], filtration of contaminants [30,31], and the additive manufacturing of complex fluid networks [32] or thermal management [33].

2. Materials and Methods

2.1 Device Fabrication

Our device is designed using AutoCad and printed as a mask onto a transparent plastic sheet (CAD/Art Services). The channel consisted of main channel (750 μm wide and 17 mm long) along with a side channel (20 μm wide and 3 mm long) for injection of the fluorescent dye. The porous

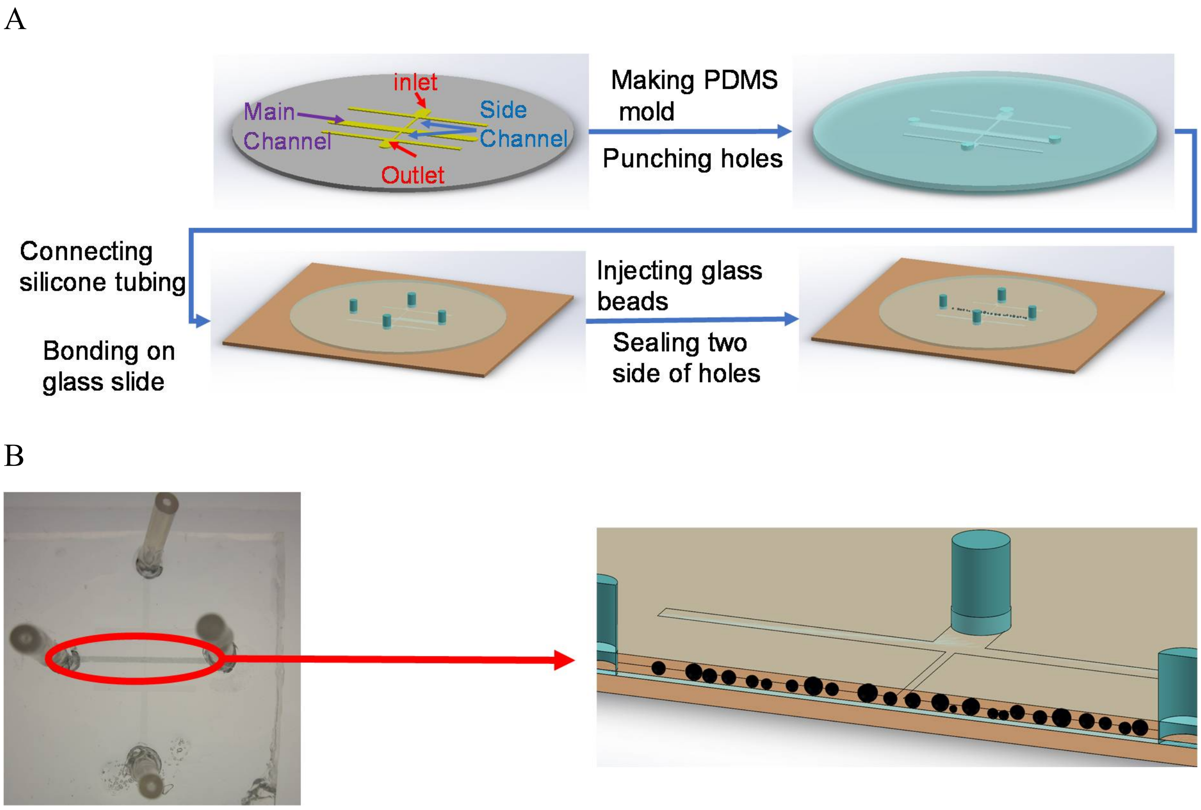

Figure 1 – A) The design of the microfluidic device used in this work along with the procedures used to fabricate the channel. B) A photograph of the microfluidic device with a schematic that illustrates how where glass beads are packed in to form a porous structure.

media is assembled from a glass beads packed within the main channel. The fabrication process, shown in Figure 1A, begins with conventional photolithography used to transfer the pattern from the mask to a 4-inch silicon wafer (University Wafer) using photoresist (SU8 2050, Microchem). The photoresist thickness is approximately 54 μm based on profilometry measurements.

Once the pattern has been produced onto a silicon substrate through photolithography, it is transferred to a polystyrene petri dish into which polydimethylsiloxane (PDMS, Sylgard 184, Dow Corning) is poured to form a mold. The PDMS is mixed with a ratio of 10:1 monomer to curing agent by weight. After pouring the uncured PDMS over the pattern, the mold in placed in a desiccator, where air bubbles are removed from the mold using a vacuum pump. The mold is placed into an oven to cure for 2 hours at 60°C. The cured mold is then removed from the silicon master using a razor, and 3 mm diameter holes are opened at the channel ends with a biopsy punch to create injection points for the fluids.

The PDMS microfluidic device is bonded to a microscope slide (Fisher Scientific, Catalog# 12-550C) that is washed in acetone and methanol to remove organic debris, after which the solvent is washed off the slide with deionized water (ARIES High Purity Water System, Aries Filterworks) and the slide is dried with nitrogen. Dust debris is removed from the PDMS using adhesive office tape, after which the microscope slide and the PDMS are placed inside a plasma cleaner (Harrick Plasma, PDC-32G) and treated for 2 minutes. The PDMS and the microscope slide are then placed in contact with one another before being heated at 60°C for around 2 hours to improve sealing. The microfluidic

Peer-reviewed version available at Colloids Interfaces 2018, 2, 23; doi:10.3390/colloids2020023

device is then removed from the oven and silicone tubing (Saint-Gobain, Version SPX-50, Product#ABX00001) is inserted through the 3 mm holes, with a small amount of PDMS placed around the tubing perimeter to ensure a firm seal. The device is finally placed back in the oven for 1 hour to cure.

The porous media is formed using randomly close-packed soda lime glass microspheres (P2050SL-2.5 35-45µm - 1kg, Cospheric). Sieves with 38 µm, 45 µm and 63 µm meshes are used to separate the glass microspheres and achieve a diameter range of ~48-63 µm after several rounds of sieving. Since the diameter of our microspheres is larger than the side channels used to inject our aqueous phase, we expect the microspheres to remain in place. A laboratory scale (LW Measurements, Model# HRB224) is used to weigh samples of 0.15 grams of glass microspheres, which are dispersed in 20 mL of DI water and pumped into the large microchannel using a syringe pump (GenieTouch, Kent Scientific) until the channel is filled with glass microspheres. After introducing the glass microspheres, the device is placed in an oven for 8 hours to evaporate excess water, making it ready for use. The device was weighed both before and after the injection process to determine the amount of glass microspheres injected into the device. This mass measurement is used with an estimate for the average microsphere radius (~55.5 µm) to calculate the total volume occupied by the glass microspheres. This measurement provides an estimate for the porosity of the structure formed by the packed glass microspheres which we found to be comparable to calculations of porosity based on image analysis. The porosity value that we obtain from these two values only has 5% different between both measurements.

2.2 Image Capture and Processing

Experimental observations of water injection are accomplished using an Olympus IX70 microscope with a 10X objective lens. A scientific CMOS camera (Optimos, QImaging) is used to record video and capture images (480 x 270) for porosity analysis. An LED light source (wLS, QImaging) is used to illuminate the sample and excite the fluorescent dye. Video of the dye being injected into the fluid is captured at a rate of 5 frames per second. The scale for these images is 3.7281 microns per pixel.

After capturing experimental videos, we use ImageJ to crop the videos and retain the main channel where the oil displacement occurs. These videos and then analyzed using a program written in MATLAB to track changes in fluorescence due to aqueous phase invasion. The program applies a boxcar filter to reduce the image noise. A threshold value for each frame of the video is calculated to retain the area occupied by the fluorescent dye. This area is compared to unoccupied area to obtain the degree of water saturation. This result is also used to obtain the fractal dimension of the aqueous phase.

2.3 Device Characterization

MATLAB code [34,35], initially developed to measure porosity and pore radius for thin rock samples, was adapted to provide a more accurate measure of porosity. Before performing an experiment, an optical image was taken of the point where the main channel meets with the dye injection port (Figure 2, top-left). After the image is converted to black and white (Figure 2, top-right), the MATLAB algorithm draws a series of test lines across the image to determine the average sizes of pore space (white) and grain size (black), with the ratio of empty pore space to total image area representing the porosity for a thin sample. The average porosity measured within the device is consistent with measurements made by weighing the device. The observed pore size is 20 μm for the test sample, while the distribution of pore sizes is shown in Figure 2. The average porosities for all of our packed beds were 0.063, 0.113 and 0.143.

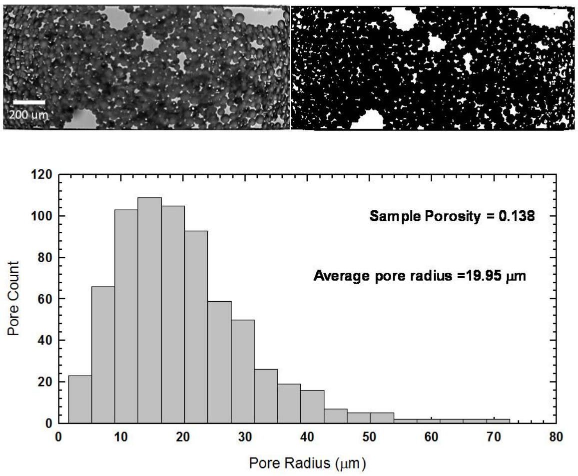

Figure 2 – A representative image of our porous structures (top, left) and a black and white image (top, right) generated during our measurement of the porosity. A sample distribution (bottom) of the pore radius for a representative image.

2.4 Experimental Details

The experiments utilized silicone oil (ν_{oil} = 5 cSt, ρ_{oil} = 0.913 g/mL) as a defending fluid. After porosity measurements are completed, silicone oil (product # 317667, Sigma Aldrich) is injected into the main channel before the main channel is sealed with PDMS to prevent leaks. Deionized water (ν_{water} = 1 cSt, ρ_{water} = 0.99 g/mL), used as the invading fluid, is injected into the microfluidic device through a side channel using a syringe pump (Chemyx Fusion 100). The mobility ratio, defined as the ratio of dynamic viscosities ($M = \nu_{oil}\,\rho_{oil} / \nu_{water}\,\rho_{water}$), is a measure of the ease with which an invading fluid flows in the presence of a defending fluid [36], with lower mobility allowing the invading fluid to flow through the porous media and recover more oil than a mobility is higher.

The capillary number [37] is $Ca = \nu_{oil}\,\rho_{oil}\,v_{inj} / \gamma$, where v_{inj} is the average velocity of the invading fluid during injection and γ is the surface tension between the two fluid phases. The characteristic injection velocity is $v_{inj} = Q / b{\cdot}d$, where Q is the injection rate, b is the gap thickness of the device (~54 μm) and d is the median pore-throat size (~15 μm). The injection rate for all experiments in this article was fixed at 0.1 mL/hr using a syringe pump. Initial experiments were conducted using deionized water containing 0.1875 mM of Rhodamine B dye sourced from ARCOS Organics. The surface tension at the silicone oil-water interface was 24.35 mN/mm based on measurements described in the literature [38]. We estimate the characteristic capillary number is approximately $6{\times}10^{-6}$.

Experiments conducted with water injection into the oil-saturated porous medium were compared to experiments in which a surfactant was introduced to reduce surface tension. Two chemical modifiers, sodium dodecyl sulfate (SDS, Sigma Aldrich, Product#75746) and polyvinylpyrrolidone (PVP, Alfa Aesar, MW 40,000, Product #J62417), were selected for comparison based on their use in the petroleum industry for enhancing oil recovery [39,40]. The fluorescent dye solution is prepared as previously described, and a surfactant or polymer with a concentration of 0.1 wt% added to this solution. Since our injection flow rate is slow, we expect that swelling of the PDMS will not influence the results [41]. The injection experiments were conducted in a manner similar to those described for water alone.

3. Theory and Simulation

Modeling two-phase fluid flow in porous media requires a coupled system of nonlinear, time-dependent partial differential equations.[42] We use an approach known as the implicit pressure, explicit saturation (IMPES) model [43] to simulate the transport of the invading water phase in our device. The model relies on an implicit formulation of conservation of mass and momentum to reduce the computational cost of the simulation [44].

The formulation of the model begins with a mass balance for an incompressible, immiscible two-phase flow [45],

$$\frac{\partial(\phi\rho_\alpha S_\alpha)}{\partial t} + \nabla\cdot(\rho_\alpha \boldsymbol{u}_\alpha) = q_\alpha \qquad \alpha = w, o \qquad \text{(Eq. 1)}$$

where ϕ is the medium porosity, ρ is the fluid density, S is the saturation, **u** is the volumetric velocity, q is the mass flow rate per unit volume, and α is the phase type (water or oil). Darcy's law is used to model the volumetric velocity of the fluid phases as they flow through the porous medium for a thin section of negligible depth,

$$\boldsymbol{u}_\alpha = -\frac{k_{r\alpha}}{\nu_\alpha\rho_\alpha}\boldsymbol{k}\nabla P_\alpha \qquad \alpha = w, o \qquad \text{(Eq. 2)}$$

where $k_{r\alpha}$ is the relative permeability, **k** is the absolute permeability tensor of the porous medium and P is pressure.

Substituting Eq. 2 into Eq. 1 and applying the assumption that porosity does not change with time yields [43],

$$-\nabla\cdot[\boldsymbol{K}\lambda_\alpha(S_\alpha)\nabla P_\alpha] = q_\alpha \qquad \alpha = w, o \qquad \text{(Eq. 3)}$$

where the parameter, λ, is referred to as the phase mobility. The saturation of the water phase is defined as,

$$\phi\frac{\partial S_w}{\partial t} + \nabla\cdot(f_w(S_w)\boldsymbol{u}) = \frac{q_w}{\rho_w} \qquad \text{(Eq. 4)}$$

where $\mathbf{u} = \mathbf{u}_w + \mathbf{u}_o$ is the total velocity of the system and $f_w = \lambda_w/(\lambda_w+\lambda_o)$ measures the fraction of water flowing through the system. Introducing a set of simple analytical expressions allows us to close the model presented by Eqs. 3 and 4,

$$\lambda_w(S_w) = \frac{(S^*)^2}{\nu_w\rho_w} \qquad \lambda_o(S_o) = \frac{(1-S^*)^2}{\nu_o\rho_o} \qquad S^* = \frac{S_w - S_{wc}}{1 - S_{or} - S_{wc}}$$

where S_{wc} is the water trapped in the pores during the formation of the porous medium and S_{or} is the lowest oil saturation that can be achieved by water displacement. The oil and water phase saturations are constrained by $S_o + S_w = 1$.

The solution to these systems of equations are based on the approach of Aarnes et al. [43] and coded in MATLAB. The simulation approach is summarized here. The model simulates a two-dimensional representation of the oil-saturated porous medium. The fluid properties (density and viscosity) mentioned in the Materials and Methods section are used to estimate the initial mobility ratio of the system. The initial oil saturation distribution is assumed to be uniform throughout our porous medium. The absolute permeability tensor, **k**, is generated using a random distribution with a log-normal profile. As the time step within the simulation advances, the pressure distribution is calculated using two-point flux approximation (TPFA) scheme to discretize the pressure equation (Eq. 3) along with edge velocities.

An explicit finite-volume formulation of the saturation equation (Eq. 4) of the form

$$S_i^{n+1} = S_i^n + (\delta_x^t)_i\left(\max(q_i, 0) - \textstyle\sum_j f(S^m)_{ij}v_{ij} + f(S_i^m)\min(q_i, 0)\right),$$

is used to advance the change in phase saturation with a dimensionless time step, $(\delta_x^t)_i$. The parameter γ_{ij} is the total flux over an edge between two adjacent cells Ω_i and Ω_j, and f_{ij} is the fractional flow function at γ_{ij}. The fractional flow function is,

$$f_w(S)_{ij} = \begin{cases} f_w(S_i) & if\ v \cdot n_{ij} \geq 0 \\ f_w(S_j) & if\ v \cdot n_{ij} < 0 \end{cases}$$

(Eq.5)

The model presented here is used to directly compare to experimental results. This done by taking the ensemble average of the water phase saturation, $\langle S_w \rangle = N^{-1} \sum_{i=1}^{N} S_{w,i}$, across the simulation domain with N elements (i.e., total numbers of grid blocks) as a function of simulation time. The results are converted to experimental time, which allow for a direct comparison to experimental results. The ensemble average of experimentally observed water saturation is directly measured by identifying the area occupied by the Rhodamine B dye. We obtain a coefficient of determination through water phase saturation to determine the goodness of fit for the simulation.

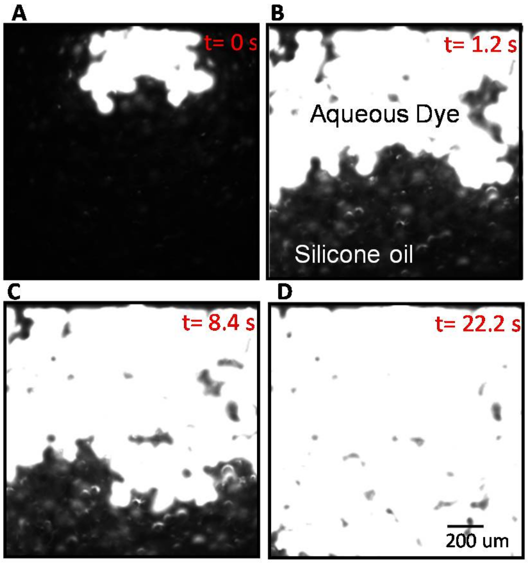

Figure 3 – A representative experiment for water with 0.1% SDS at a porosity of 0.143. Initially (A), the main channel full of silicone oil which is black. When the water phase invades the main channel, rhodamine B is used to track the displacement of silicone oil (B and C) until the whole main channel fluoresces (D). In this figure, the white represents rhodamine B and black represents silicone oil.

If the coefficient of determination (COD) is below a value of $r^2 = 0.9$, we run a series of forward simulations to try and improve the fit to our data. Mobility is used as an adjustable parameter as a way to account for mixing [46] between phases. The mobility for the next forward simulation is drawn from a uniform probability distribution,

$$M_{i+1} = M_f[1 + (2\xi - 1)\delta]$$

where M_f is the mobility ratio associated with the best COD, M_{i+1} is the mobility for the next forward simulation, and ξ is a random uniform number that ranges from 0 to 1 and δ is a maximum possible range parameter, which we set to a value of 0.1. The new COD value is compared to the old COD value when the simulation is complete. The factor, M_f, remains unchanged if the new COD is lower than the old COD. Otherwise, we update $M_f = M_{i+1}$ if the COD value is found to improve.

4. Results and Discussion

4.1 Oil displacement efficiency

The experimental displacement of silicone oil by waterflooding is illustrated in Figure 3. The rhodamine-dyed water initially builds up sufficient pressure at the inlet port to break through into

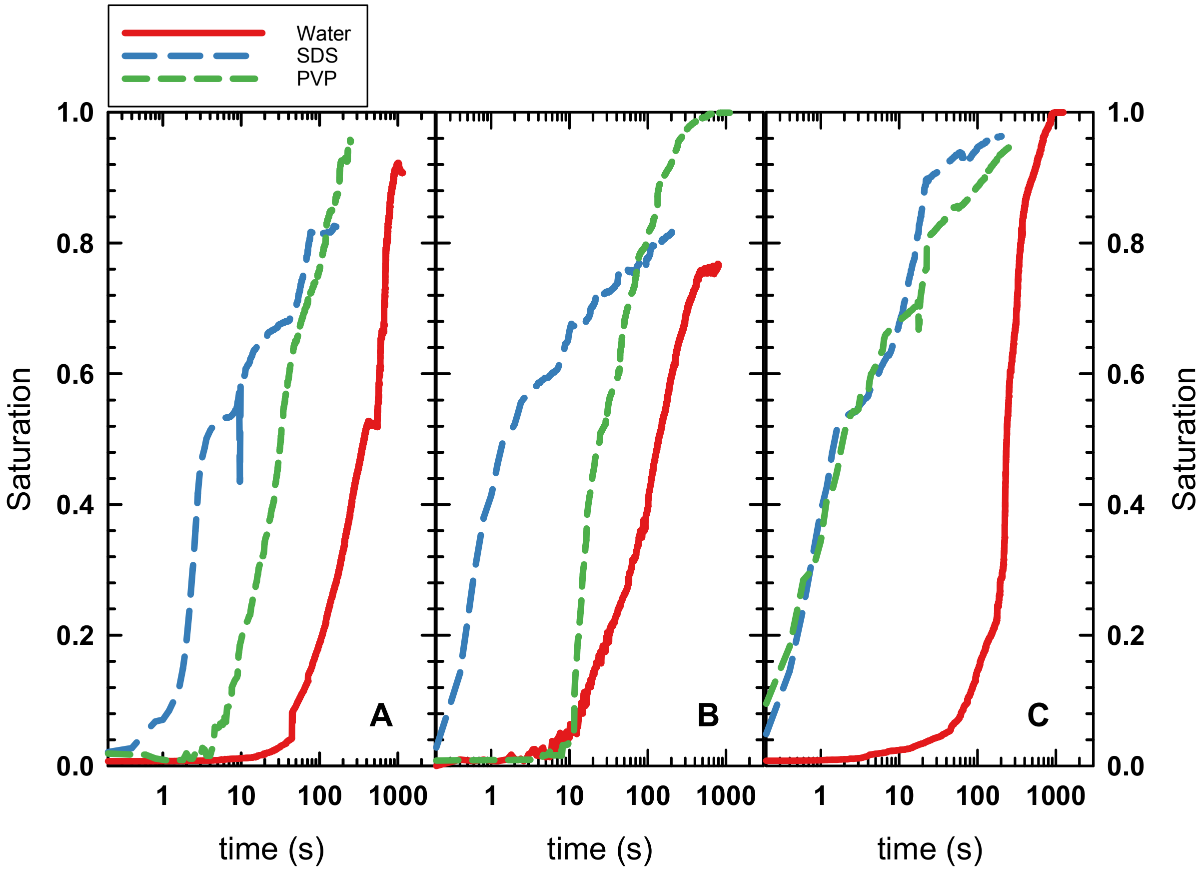

Figure 4 – The relationship between saturation of an invading water phase for three water-based fluids (no surfactant, 0.1% SDS and 0.1% PVP) as they displace oil from a packed bed of glass microspheres with porosity of 0.063 (A), 0.113 (B) and 0.143 (C).

the porous media micromodel. As the water displaces silicone oil, some silicone oil still remain in voids (Figures 3B and C) and, after approximately 20 seconds, the water reaches the exit port on the opposite side of the porous media micromodel (Figure 3D). Observing the porous media micromodel after the initial exit of the water, we see a reduction in void size over time as additional silicone oil is either displaced by water or shrinks due to the applied pressure of the flow.

We performed three separate types of waterflooding experiments similar to the one described in Figure 3. The first type of experiment used water mixed only with rhodamine, while the other two types of experiments utilized SDS or PVP (Figure 4). A packed bed of glass beads was prepared before each experiment and characterized using the previously described protocol. MATLAB image analysis code was written to track the area occupied by the rhodamine dye during the experiment, allowing estimation of the average water phase saturation defined by $S_w = A_{dye} / A_{channel}$.

Figure 4 shows the results of our waterflooding experiments, both for the presence and the absence of surfactant or polymer. Three separate packed beds of different porosities (0.063, 0.113 and 0.143) were prepared for each fluid type, and Figure 4A shows the results for a media with porosity 0.063. The water-bearing SDS initially invades the packed bed faster than either the water-bearing

PVP or water alone could do. The SDS reduces the oil-water interfacial tension more significantly than PVP and water alone, which we illustrate by a contact angle measurement. An image analysis method was adapted to measure the contact angle at the oil-water interface in our microfluidic channel [47]. The measured contact angles were 42.9° ± 1.4° and 22.3° ± 0.9° for the SDS and PVP solutions, respectively. Water was measured to have a contact angle of 11.2° ± 0.9° in the absence of a surfactant or polymer. The contact angle for water in the microchannel is similar to contact angle values reported for plasma-treated PDMS surfaces [48–50]. While the SDS solution initially invades the oil phase at a faster rate in Figure 4A, the PVP solution typically saturates the porous media to a more significant degree after a longer period of time.

The experiment shown in Figure 4B was conducted for a packed bed with porosity 0.113. As in Figure 4A, the water-bearing PVP solution achieves a higher saturation than SDS or water alone and invasion by both surfactant solutions occurred faster than for water alone at this porosity. For the highest porosity value (0.143 in Figure 4C), water alone achieved the highest level of saturation compared to values at the lower porosities, although its rate of invasion slower than the surfactant solutions. Both the PVP and SDS solutions invaded at comparable rates at the highest porosity, with SDS saturating the porous bed to a slightly greater extent than the PVP solution.

4.2 Fractal dimension

We used image analysis to evaluate the fractal dimension of the area occupied by the by the fluorescent dye in our microfluidic device fluorescent dye in our microfluidic device to better understand the oil displacement kinetics. A MATLAB code was adapted to evaluate the fractal dimension using the Hausdorff technique [51], where a series of boxes are drawn within the region containing the dye. The bright pixels within each box are counted and compared to the total number of boxes drawn by the code. The values obtained by this analysis provide a measure of the fractal dimension for the area occupied by the water. The results of the image analysis (Figure 5A-C) show that water and the PVP solution begin with a fractal dimension of $D_f \sim 1.2$ or less, representing structures classified as stringy [52]. At the lowest (0.063, Figure 5A) and highest (0.143, Figure 5C) porosity levels, it takes about 100 s for the water to occupy an area that morphologically resembles a fractal ($D_f \sim 1.6$).

The only exception to this transition in morphology is the channel with porosity 0.11 (Figure 5C), for which the evolution takes place over a period of time approximately half that of the other data sets. The SDS solution also exhibits different morphological behavior than the other solutions, achieving a fractal morphology on a short timescale (~ 1 s or less), indicating that these solutions invade oil-saturated pore spaces at a far easier rate than the other solutions. All solutions achieved a final fractal dimension of $D_f \sim 1.89$, indicating that fluid had percolated [53] through the packed bed in the microchannel.

The fractal dimension is connected to the area saturated by the invading fluid through its radius of gyration [54]. The radius of gyration represents a measure of the extent to which the invading fluid has displaced the oil in the porous medium and is defined as [55],

$$R_g = \sqrt{M_{2x} + M_{2y}}$$

where

Peer-reviewed version available at *Colloids Interfaces* **2018**, *2*, 23; doi:10.3390/colloids2020023

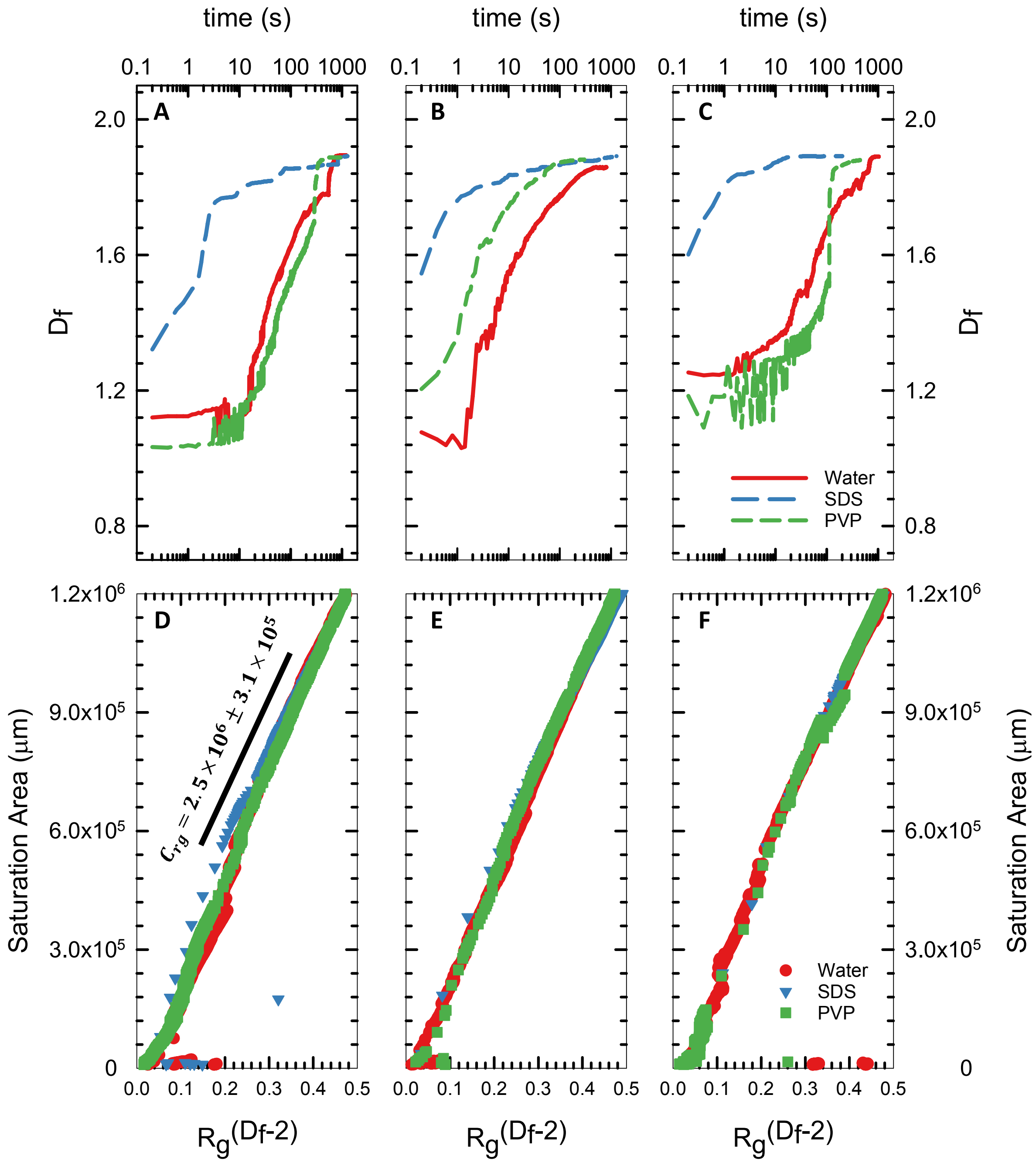

Figure 5 – The Hausdorff fractal dimension (A-C) as a function of time was evaluated using image analysis. The results in A-C show that, while all the samples evolve differently with time, they reach a point where they are topologically similar. Combining the fractal dimension with radius of gyration (D-F) reveal that all samples scale linearly with the saturation area.

$$M_{2x} = \frac{1}{S}\sum_{i=1}^{N}(x_i - M_{1x})^2 \quad M_{2y} = \frac{1}{S}\sum_{i=1}^{N}\left(y_i - M_{1y}\right)^2 \text{ and } M_{1x} = \frac{1}{A_w}\sum_{i=1}^{N} x_i \quad M_{1y} = \frac{1}{A_w}\sum_{i=1}^{N} y_i$$

where A_w is the measured area occupied by the invading water phase, N is the number of pixels making up the pattern as recorded by the CMOS camera, and x_i and y_i are the coordinates of each pixel in the observed pattern. We find that the relationship between area and radius of gyration is well described by $A_w = C_{rg}R_g^{(D_f-2)}$, where D_f is a function of time, as shown in Figures 5A-C. The

		Water		0.1% SDS		0.1% PVP	
		A_{max} (µm^2) / 10^6	t_c (s)	A_{max} (µm^2) / 10^6	t_c (s)	A_{max} (µm^2) / 10^6	t_c (s)
Porosity	0.063	1.266	86.2	1.105	17.6	1.253	285.7
	0.11	1.059	111.1	1.241	11.0	1.209	25.3
	0.143	1.258	357.1	1.269	2.1	1.209	10.4

Table 1 – Fitting parameters for A_{max} and time constant of the three water-based fluid systems examined in this work.

relationship between area, radius of gyration and fractal dimension proposed here is similar to previously proposed models for diffusion limited viscous fingering in porous media [56]. By comparing data from all nine porosities examined in this work, we find that the data collapses to a single curve when $C_{rg} = 2.5\times10^6 \pm 3.1\times10^5$, where A_w and R_g are in units of microns (see Figure 5 D-F).

While the fractal dimension can help us identify morphological differences in the way an invading fluid phase spreads, and we would also like to observe differences in rate of invasion (dA_w/dt). Numerical calculation of the rate of invasion from image analysis data is challenging since noise in the data can create artifacts that suggest unrealistically large fluctuations in invasion rate. To minimize the effect of such artifacts, we chose to fit the area data to a model, $A_w = A_{w,max}\left(1 - e^{-t/t_c}\right)$, that is consistent with expected behavior of oil recovered through water injection into porous reservoirs.[57] The parameter, $A_{w,max}$, is the maximum area occupied by the water during the experiment and t_c is the time constant of the experiment.

Table 1 summarizes the results of fitting an exponential rise to a maximum for our area data as a function of time. The average value of the area parameter is $A_{w,max} = 1.208\times10^6 \pm 7.5\times10^4$ µm^2, with the small standard deviation indicating that there is no significant difference between samples based on maximum area occupied by the invading water phase. We do find that there are significant differences in time constants for the samples we examined, with the water samples exhibiting more than a 4-fold increase in time constant with increasing porosity. The time constants for SDS and PVP-bearing solutions exhibit an opposite trend, i.e., a decrease in time constant with increasing porosity. This suggests that the polymer and surfactant solutions make it easier to fill larger void volumes when compared to water alone.

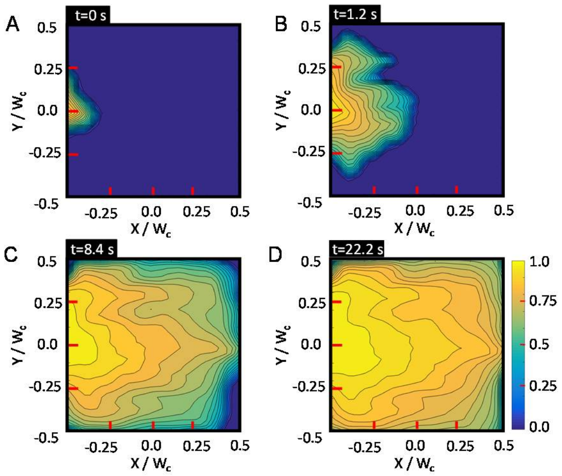

Figure 6 – An IMPES simulation for the case with 0.1% SDS in water. Snapshots are taken at intervals that correspond to Figure 3. The color bar shows the value for the local saturation.

4.3 IMPES

We implemented an inverse IMPES simulation to be compared to our experimental results. Figure 6 shows a sample simulation result for 0.1% SDS,

Peer-reviewed version available at Colloids Interfaces 2018, 2, 23; doi:10.3390/colloids2020023

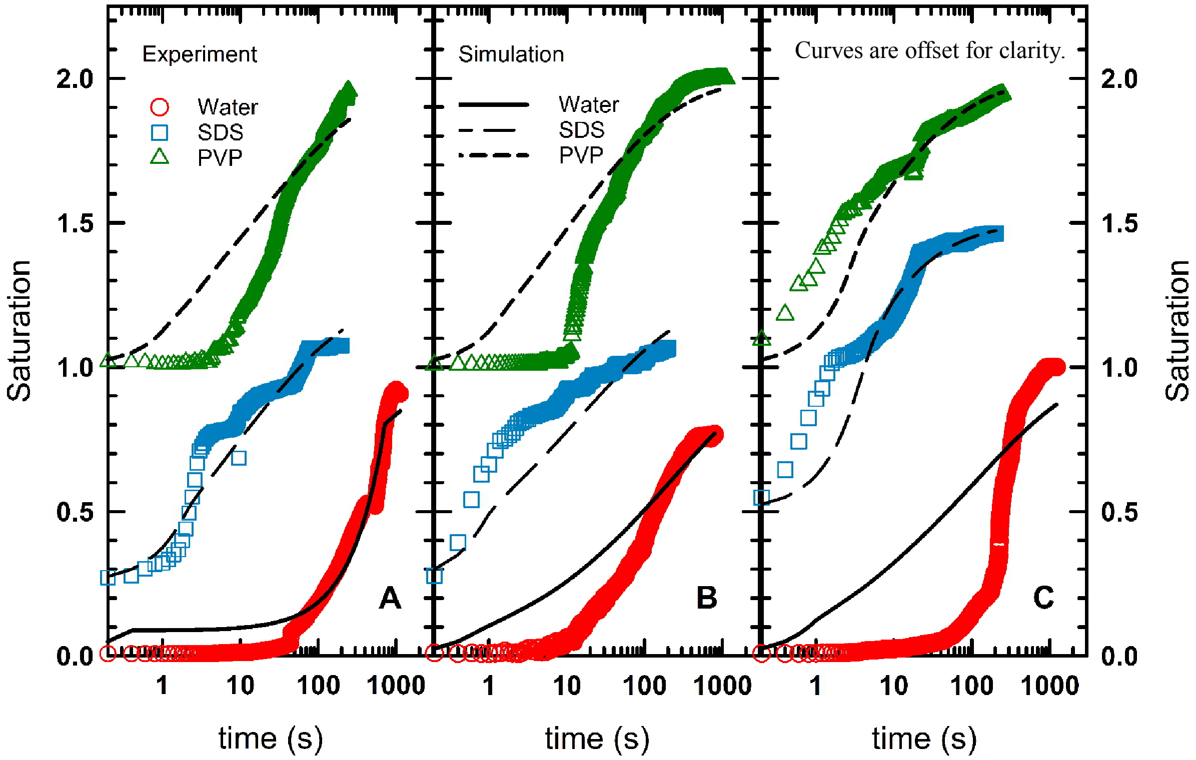

Figure 7 – A comparison of our experimental results to an IMPES simulation of oil displacement by an invading water phase in a medium with porosity of 0.063 (A), 0.113 (B) and 0.143 (C). The saturation curves are offset from each other for better clarity.

matching the conditions observed in Figure 3. The key differences between results of our simulations and the experiment is that the simulation results show the invasion initially occurring at a slightly slower rate that in the actual experiment (Figures 6A and 6B), and near the midpoint of the simulation (Figure 6C), the invading phase breaks through and occupies a wider region than that at the comparable experimental time (Figure 3C). We attribute these differences to the way our IMPES simulation models do not count interface tension effect. To mimic the structure of the randomly packed spheres, we modeled the permeability using values drawn from a log-normal distribution [43], although the procedure is designed to model porous rock rather than a packed bed of spheres.

Despite these differences, the average saturation curves obtained by simulation closely match our experimental curves (Figure 7) with high coefficients of determination for most of these curves (Table 2). The mobility ratios that best fit the data exhibit decreases with increasing porosity both for water and 0.1% PVP, indicating that these phases move through the porous packed bed easier at higher porosities. The mobility ratios for 0.1% SDS deviate from this trend; at a porosity of 0.113, the 0.1% SDS appears to have a mobility of 33.3. While the coefficient of determination was low for this this case, the simulation did capture the general saturation trend as a function of time. Overall, our simulations do show that the addition of SDS or PVP improves the mobility of the water phase as it

	Water			SDS			PVP		
Porosity	0.063	0.113	0.143	0.063	0.113	0.143	0.063	0.113	0.143
Mobility	255.8	114.7	87.2	11.2	33.3	1.9	18.2	12.5	4.6
R^2	0.95	0.87	0.54	0.87	0.29	0.88	0.8	0.79	0.87

Table 2 – The mobility ratio that best fit the experimental data and the coefficient of determination (R^2) associated with each fit.

invades an oil-saturated medium, and except for the 0.113 case, SDS exhibits lower mobility ratios than PVP for the experiments conducted here.

5. Conclusions

We developed a microfluidic platform by which the waterflooding of an oil-saturated porous structure is investigated through optical fluorescence microscopy. Where the characterization of bulk porous media is rate limited [10,11], our microfluidic platform is able to characterize the invasion of a water phase into an oil-saturated medium within a relatively short amount of time. The flexibility of this platform allows us to rapidly analyze chemical modification techniques that are commonly used in the petroleum industry [39,40] to enhance the recovery of oil. Observations of our device using optical fluorescence microscopy enables us to track the invasion of a water phase into an oil saturated phase and evaluate parameters such as saturation [58–60], fractal morphology [52,54,61], temporal evolution of flow patterns [62,63] and invasion rate [64,65] that are important for evaluating the effectiveness of different types of surfactants used for waterflooding. A simulation based on the IMPES approach [42,43,45] for modeling two-phase flow in porous media was implemented in MATLAB [43] to perform an inverse analysis of our experimental data to estimate the mobility of the invading phase. The results of our inverse analysis demonstrate a significant decrease in mobility for water bearing a polymer or surfactant.

The analysis performed in this article will form the basis of future work aimed at characterizing the effect surface tension has in our microfluidic platform. Our IMPES model will be adjusted by using closure expressions [66] for saturation curves that incorporate surface tension as it influences capillary pressure. We also aim to control the porosity of our system through photolithography techniques [13,26]. The approach we have used here can be used to evaluate other enhanced oil recovery systems, including other types of polymers or surfactants [67], nanoparticles [68,69], and foams [70,71]. Our platform can also be applied to other porous media situations that involve diffusion and transport in biomedical systems [32,72], carbon sequestration [73,74] and additive manufacturing of complex fluid networks [33,75,76].

Acknowledgments: JJJ acknowledges financial support from the Iowa State University Department of Mechanical Engineering. HLY and JJJ thank Min Lin and the Keck Microfabrication Facility at Iowa State University for providing photolithography support for this project. We also thank Ashton Archer and Prof. Ted Heindel for providing us access to a sieve machine for separating our glass microparticles based on size.

Peer-reviewed version available at *Colloids Interfaces* **2018**, *2*, 23; doi:10.3390/colloids2020023

References

1. Karadimitriou, N. K.; Hassanizadeh, S. M. A Review of Micromodels and Their Use in Two-Phase Flow Studies. *Vadose Zone J.* **2012**, *11*, vzj2011.0072, doi:10.2136/vzj2011.0072.
2. Muggeridge, A.; Cockin, A.; Webb, K.; Frampton, H.; Collins, I.; Moulds, T.; Salino, P. Recovery rates, enhanced oil recovery and technological limits. *Phil Trans R Soc A* **2014**, *372*, 20120320, doi:10.1098/rsta.2012.0320.
3. Blunt, M.; Fayers, F. J.; Orr, F. M. Carbon dioxide in enhanced oil recovery. *Energy Convers. Manag.* **1993**, *34*, 1197–1204, doi:10.1016/0196-8904(93)90069-M.
4. Raffa, P.; Broekhuis, A. A.; Picchioni, F. Polymeric surfactants for enhanced oil recovery: A review. *J. Pet. Sci. Eng.* **2016**, *145*, 723–733, doi:10.1016/j.petrol.2016.07.007.
5. Sagi, A. R. Surfactant Enhanced Oil Recovery. PhD Thesis, Rice University, 2015.
6. Hirasaki, G.; Miller, C. A.; Puerto, M. Recent Advances in Surfactant EOR. *SPE-115386-PA* **2011**, doi:10.2118/115386-PA.
7. Ezell, R. G.; McCormick, C. L. Electrolyte- and pH-responsive polyampholytes with potential as viscosity-control agents in enhanced petroleum recovery. *J. Appl. Polym. Sci.* **2007**, *104*, 2812–2821, doi:10.1002/app.24999.
8. Rashidi, M.; Blokhus, A. M.; Skauge, A. Viscosity study of salt tolerant polymers. *J. Appl. Polym. Sci.* **2010**, NA-NA, doi:10.1002/app.32011.
9. Elraies, K. A.; Tan, I. M.; Fathaddin, M. T.; Abo-Jabal, A. Development of a New Polymeric Surfactant for Chemical Enhanced Oil Recovery. *Pet. Sci. Technol.* **2011**, *29*, 1521–1528, doi:10.1080/10916460903581427.
10. Morrow, N. R.; Mason, G. Recovery of oil by spontaneous imbibition. *Curr. Opin. Colloid Interface Sci.* **2001**, *6*, 321–337.
11. Standnes, D. C.; Austad, T. Wettability alteration in chalk: 2. Mechanism for wettability alteration from oil-wet to water-wet using surfactants. *J. Pet. Sci. Eng.* **2000**, *28*, 123–143.
12. Blunt, M.; King, M. J.; Scher, H. Simulation and theory of two-phase flow in porous media. *Phys. Rev. A* **1992**, *46*, 7680–7699, doi:10.1103/PhysRevA.46.7680.
13. Berejnov, V.; Djilali, N.; Sinton, D. Lab-on-chip methodologies for the study of transport in porous media: energy applications. *Lab. Chip* **2008**, *8*, 689–693, doi:10.1039/B802373P.
14. Chatenever, A.; Calhoun, J. C. Visual Examinations of Fluid Behavior in Porous Media - Part I. *J. Pet. Technol.* **1952**, *4*, 149–156, doi:10.2118/135-G.
15. Krummel, A. T.; Datta, S. S.; Münster, S.; Weitz, D. A. Visualizing multiphase flow and trapped fluid configurations in a model three-dimensional porous medium. *AIChE J.* **2013**, *59*, 1022–1029, doi:10.1002/aic.14005.
16. Zhang, C.; Kang, Q.; Wang, X.; Zilles, J. L.; Müller, R. H.; Werth, C. J. Effects of pore-scale heterogeneity and transverse mixing on bacterial growth in porous media. *Environ. Sci. Technol.* **2010**, *44*, 3085–3092.
17. Willingham, T.; Zhang, C.; Werth, C. J.; Valocchi, A. J.; Oostrom, M.; Wietsma, T. W. Using dispersivity values to quantify the effects of pore-scale flow focusing on

enhanced reaction along a transverse mixing zone. *Adv. Water Resour.* **2010**, *33*, 525–535, doi:10.1016/j.advwatres.2010.02.004.

18. Willingham, T. W.; Werth, C. J.; Valocchi, A. J. Evaluation of the Effects of Porous Media Structure on Mixing-Controlled Reactions Using Pore-Scale Modeling and Micromodel Experiments. *Environ. Sci. Technol.* **2008**, *42*, 3185–3193, doi:10.1021/es7022835.
19. Lenormand, R.; Touboul, E.; Zarcone, C. Numerical models and experiments on immiscible displacements in porous media. *J. Fluid Mech.* **1988**, *189*, 165–187, doi:10.1017/S0022112088000953.
20. Ferer, M.; Ji, C.; Bromhal, G. S.; Cook, J.; Ahmadi, G.; Smith, D. H. Crossover from capillary fingering to viscous fingering for immiscible unstable flow: Experiment and modeling. *Phys. Rev. E* **2004**, *70*, doi:10.1103/PhysRevE.70.016303.
21. Cottin, C.; Bodiguel, H.; Colin, A. Drainage in two-dimensional porous media: From capillary fingering to viscous flow. *Phys. Rev. E* **2010**, *82*, doi:10.1103/PhysRevE.82.046315.
22. Lenormand, R.; Zarcone, C.; Sarr, A. Mechanisms of the displacement of one fluid by another in a network of capillary ducts. *J. Fluid Mech.* **1983**, *135*, 337–353, doi:10.1017/S0022112083003110.
23. Chang, L.-C.; Tsai, J.-P.; Shan, H.-Y.; Chen, H.-H. Experimental study on imbibition displacement mechanisms of two-phase fluid using micro model. *Environ. Earth Sci.* **2009**, *59*, 901, doi:10.1007/s12665-009-0085-6.
24. Theodoropoulou, M. A.; Sygouni, V.; Karoutsos, V.; Tsakiroglou, C. D. Relative permeability and capillary pressure functions of porous media as related to the displacement growth pattern. *Int. J. Multiph. Flow* **2005**, *31*, 1155–1180, doi:10.1016/j.ijmultiphaseflow.2005.06.009.
25. Berejnov, V.; Djilali, N.; Sinton, D. Lab-on-chip methodologies for the study of transport in porous media: energy applications. *Lab. Chip* **2008**, *8*, 689, doi:10.1039/b802373p.
26. Wu, M.; Xiao, F.; Johnson-Paben, R. M.; Retterer, S. T.; Yin, X.; Neeves, K. B. Single- and two-phase flow in microfluidic porous media analogs based on Voronoi tessellation. *Lab. Chip* **2011**, *12*, 253–261, doi:10.1039/C1LC20838A.
27. Xiao, F.; Yin, X. Geometry models of porous media based on Voronoi tessellations and their porosity–permeability relations. *Comput. Math. Appl.*, doi:10.1016/j.camwa.2015.09.009.
28. Marchand, S.; Bondino, I.; Ktari, A.; Santanach-Carreras, E. Consideration on Data Dispersion for Two-Phase Flow Micromodel Experiments. *Transp. Porous Media* **2017**, *117*, 169–187, doi:10.1007/s11242-017-0827-y.
29. Ghesmat, K.; Hassanzadeh, H.; Abedi, J. The impact of geochemistry on convective mixing in a gravitationally unstable diffusive boundary layer in porous media: CO2 storage in saline aquifers. *J. Fluid Mech.* **2011**, *673*, 480–512, doi:10.1017/S0022112010006282.

Peer-reviewed version available at *Colloids Interfaces* **2018**, *2*, 23; doi:10.3390/colloids2020023

30. Kersting, A. B.; Efurd, D. W.; Finnegan, D. L.; Rokop, D. J.; Smith, D. K.; Thompson, J. L. Migration of plutonium in ground water at the Nevada Test Site. *Nature* **1999**, *397*, 56–59, doi:10.1038/16231.
31. Jensen, K. H.; Valente, A. X. C. N.; Stone, H. A. Flow rate through microfilters: Influence of the pore size distribution, hydrodynamic interactions, wall slip, and inertia. *Phys. Fluids* **2014**, *26*, 052004, doi:10.1063/1.4876937.
32. Miller, J. S.; Stevens, K. R.; Yang, M. T.; Baker, B. M.; Nguyen, D.-H. T.; Cohen, D. M.; Toro, E.; Chen, A. A.; Galie, P. A.; Yu, X.; Chaturvedi, R.; Bhatia, S. N.; Chen, C. S. Rapid casting of patterned vascular networks for perfusable engineered three-dimensional tissues. *Nat. Mater.* **2012**, *11*, 768–774, doi:10.1038/nmat3357.
33. Marschewski, J.; Brenner, L.; Ebejer, N.; Ruch, P.; Michel, B.; Poulikakos, D. 3D-printed fluidic networks for high-power-density heat-managing miniaturized redox flow batteries. *Energy Environ. Sci.* **2017**, *10*, 780–787, doi:10.1039/C6EE03192G.
34. Rabbani, A.; Jamshidi, S. Specific surface and porosity relationship for sandstones for prediction of permeability. *Int. J. Rock Mech. Min. Sci.* **2014**, *71*, 25–32, doi:10.1016/j.ijrmms.2014.06.013.
35. Rabbani, A.; Jamshidi, S.; Salehi, S. Determination of Specific Surface of Rock Grains by 2D Imaging. *J. Geol. Res.* **2014**, *2014*, 1–7, doi:10.1155/2014/945387.
36. Kumar, M.; Hoang, V. T.; Satik, C.; Rojas, D. H. High-Mobility-Ratio Waterflood Performance Prediction: Challenges and New Insights. *SPE Reserv. Eval. Eng.* **2008**, *11*, 186–196, doi:10.2118/97671-PA.
37. Lenormand, R.; Touboul, E.; Zarcone, C. Numerical models and experiments on immiscible displacements in porous media. *J. Fluid Mech.* **1988**, *189*, 165, doi:10.1017/S0022112088000953.
38. Than, P.; Preziosi, L.; Joseph, D. D.; Arney, M. Measurement of interfacial tension between immiscible liquids with the spinning road tensiometer. *J. Colloid Interface Sci.* **1988**, *124*, 552–559, doi:10.1016/0021-9797(88)90191-9.
39. Stahl, G. A.; Schulz, D. N. *Water-Soluble Polymers for Petroleum Recovery*; 1988 edition.; Springer: New York, 1988; ISBN 978-0-306-42915-6.
40. Taylor, K. C.; Nasr-El-Din, H. A. Water-soluble hydrophobically associating polymers for improved oil recovery: A literature review. *J. Pet. Sci. Eng.* **1998**, *19*, 265–280, doi:10.1016/S0920-4105(97)00048-X.
41. Gervais, T.; El-Ali, J.; Günther, A.; Jensen, K. F. Flow-induced deformation of shallow microfluidic channels. *Lab. Chip* **2006**, *6*, 500, doi:10.1039/b513524a.
42. Kou, J.; Sun, S. On iterative IMPES formulation for two phase flow with capillarity in heterogeneous porous media. *Int. J. Numer. Anal. Model. Ser. B* **2010**, *1*, 20–40.
43. Aarnes, J. E.; Gimse, T.; Lie, K.-A. An Introduction to the Numerics of Flow in Porous Media using Matlab. In *Geometric Modelling, Numerical Simulation, and Optimization*; Applied Mathematics at SINTEF.
44. Li, B.; Chen, Z.; Huan, G. Comparison of solution schemes for black oil reservoir simulations with unstructured grids. *Comput. Methods Appl. Mech. Eng.* **2004**, *193*, 319–355, doi:10.1016/j.cma.2003.09.012.

Peer-reviewed version available at *Colloids Interfaces* **2018**, *2*, 23; doi:10.3390/colloids2020023

45. Chen, Z.; Huan, G.; Li, B. An Improved IMPES Method for Two-Phase Flow in Porous Media. *Transp. Porous Media* **2004**, *54*, 361–376, doi:10.1023/B:TIPM.0000003667.86625.15.
46. Habermann, B. The Efficiency of Miscible Displacement as a Function of Mobility Ratio. *Trans. Am. Inst. Min. Metall. Eng.* **1960**, *219*, 264–272.
47. Matlab Central Measuring Angle of Intersection - MATLAB & Simulink Example Available online: https://www.mathworks.com/help/images/examples/measuring-angle-of-intersection.html (accessed on Apr 6, 2018).
48. Fritz, J. L.; Owen, M. J. Hydrophobic Recovery of Plasma-Treated Polydimethylsiloxane. *J. Adhes.* **1995**, *54*, 33–45, doi:10.1080/00218469508014379.
49. Bhattacharya, S.; Datta, A.; Berg, J. M.; Gangopadhyay, S. Studies on surface wettability of poly(dimethyl) siloxane (PDMS) and glass under oxygen-plasma treatment and correlation with bond strength. *J. Microelectromechanical Syst.* **2005**, *14*, 590–597, doi:10.1109/JMEMS.2005.844746.
50. Bodas, D.; Khan-Malek, C. Formation of more stable hydrophilic surfaces of PDMS by plasma and chemical treatments. *Microelectron. Eng.* **2006**, *83*, 1277–1279, doi:10.1016/j.mee.2006.01.195.
51. Matlab Central Hausdorff (Box-Counting) Fractal Dimension - File Exchange - MATLAB Central Available online: http://www.mathworks.com/matlabcentral/fileexchange/30329-hausdorff--box-counting--fractal-dimension (accessed on Nov 21, 2017).
52. Zhong-can, O.-Y.; Gang, Y.; Hao Bai-lin From fractal to dendritic: Competition between diffusion and field. *Phys. Rev. Lett.* **1986**, *57*, 3203–3205, doi:10.1103/PhysRevLett.57.3203.
53. Witten, T. A.; Sander, L. M. Diffusion-limited aggregation. *Phys. Rev. B* **1983**, *27*, 5686–5697, doi:10.1103/PhysRevB.27.5686.
54. Gharbi, R. B. C.; Qasem, F.; Peters, E. J. A relationship between the fractal dimension and scaling groups of unstable miscible displacements. *Exp. Fluids* **2001**, *31*, 357–366, doi:10.1007/s003480100278.
55. Pons, M.-N.; Weisser, E. M.; Vivier, H.; Boger, D. V. Characterization of viscous fingering in a radial Hele-Shaw cell by image analysis. *Exp. Fluids* **1999**, *26*, 153–160, doi:10.1007/s003480050274.
56. Maloy, K. J.; Boger, F.; Feder, J.; Jossang, T.; Meakin, P. Dynamics of viscous-fingering fractals in porous media. *Phys. Rev. A* **1987**, *36*, 318–324, doi:10.1103/PhysRevA.36.318.
57. Aronofsky, J. S.; Masse, L.; Natanson, S. G. A Model for the Mechanism of Oil Recovery from the Porous Matrix Due to Water Invasion in Fractured Reservoirs. **1958**.
58. Cheng, J. T.; Pyrak-Nolte, L. J.; Nolte, D. D.; Giordano, N. J. Linking pressure and saturation through interfacial areas in porous media. *Geophys. Res. Lett.* **2004**, *31*, L08502, doi:10.1029/2003gl019282.
59. Parseval, Y. D.; Pillai, K. M.; Advani, S. G. A Simple Model for the Variation of Permeability due to Partial Saturation in Dual Scale Porous Media. *Transp. Porous Media* **1997**, *27*, 243–264, doi:10.1023/A:1006544107324.

Peer-reviewed version available at *Colloids Interfaces* **2018**, *2*, 23; doi:10.3390/colloids2020023

60. Niemet, M. R.; Selker, J. S. A new method for quantification of liquid saturation in 2D translucent porous media systems using light transmission. *Adv. Water Resour.* **2001**, *24*, 651–666, doi:10.1016/S0309-1708(00)00045-2.
61. Cai, J.; Yu, B.; Zou, M.; Mei, M. Fractal analysis of invasion depth of extraneous fluids in porous media. *Chem. Eng. Sci.* **2010**, *65*, 5178–5186, doi:10.1016/j.ces.2010.06.013.
62. Zhu, T.; Waluga, C.; Wohlmuth, B.; Manhart, M. A Study of the Time Constant in Unsteady Porous Media Flow Using Direct Numerical Simulation. *Transp. Porous Media* **2014**, *104*, 161–179, doi:10.1007/s11242-014-0326-3.
63. Zheng, Z.; Guo, B.; Christov, I. C.; Celia, M. A.; Stone, H. A. Flow regimes for fluid injection into a confined porous medium. *J. Fluid Mech.* **2015**, *767*, 881–909, doi:10.1017/jfm.2015.68.
64. Martys, N.; Cieplak, M.; Robbins, M. O. Critical phenomena in fluid invasion of porous media. *Phys. Rev. Lett.* **1991**, *66*, 1058–1061, doi:10.1103/PhysRevLett.66.1058.
65. Geistlinger, H.; Ataei-Dadavi, I. Influence of the heterogeneous wettability on capillary trapping in glass-beads monolayers: Comparison between experiments and the invasion percolation theory. *J. Colloid Interface Sci.* **2015**, *459*, 230–240, doi:10.1016/j.jcis.2015.07.074.
66. Parker, J. C.; Lenhard, R. J. A model for hysteretic constitutive relations governing multiphase flow: 1. Saturation-pressure relations. *Water Resour. Res.* **1987**, *23*, 2187–2196, doi:10.1029/WR023i012p02187.
67. Wever, D. A. Z.; Picchioni, F.; Broekhuis, A. A. Polymers for enhanced oil recovery: A paradigm for structure–property relationship in aqueous solution. *Prog. Polym. Sci.* **2011**, *36*, 1558–1628, doi:10.1016/j.progpolymsci.2011.05.006.
68. Sedaghat, M. H.; Mohammadi, H.; Razmi, R. Application of SiO2 and TiO2 nano particles to enhance the efficiency of polymer-surfactant floods. *Energy Sources Part Recovery Util. Environ. Eff.* **2016**, *38*, 22–28, doi:10.1080/15567036.2012.740552.
69. Mohajeri, M.; Hemmati, M.; Shekarabi, A. S. An experimental study on using a nanosurfactant in an EOR process of heavy oil in a fractured micromodel. *J. Pet. Sci. Eng.* **2015**, *126*, 162–173, doi:10.1016/j.petrol.2014.11.012.
70. Ma, K.; Liontas, R.; Conn, C. A.; Hirasaki, G. J.; Biswal, S. L. Visualization of improved sweep with foam in heterogeneous porous media using microfluidics. *Soft Matter 8*, 10669–10675.
71. Conn, C. A.; Ma, K.; Hirasaki, G. J.; Biswal, S. L. Visualizing oil displacement with foam in a microfluidic device with permeability contrast. *Lab. Chip* **2014**, *14*, 3968–3977, doi:10.1039/c4lc00620h.
72. Klinzing, G. R.; Zavaliangos, A. A Simplified Model of Moisture Transport in Hydrophilic Porous Media With Applications to Pharmaceutical Tablets. *J. Pharm. Sci.* **2016**, *105*, 2410–2418, doi:10.1016/j.xphs.2016.05.030.
73. Szulczewski, M. L.; MacMinn, C. W.; Herzog, H. J.; Juanes, R. Lifetime of carbon capture and storage as a climate-change mitigation technology. *Proc. Natl. Acad. Sci.* **2012**, *109*, 5185–5189, doi:10.1073/pnas.1115347109.

Peer-reviewed version available at *Colloids Interfaces* **2018**, *2*, 23; doi:10.3390/colloids2020023

74. Zhao, B.; MacMinn, C. W.; Juanes, R. Wettability control on multiphase flow in patterned microfluidics. *Proc. Natl. Acad. Sci.* **2016**, *113*, 10251–10256, doi:10.1073/pnas.1603387113.
75. Osei-Bonsu, K.; Grassia, P.; Shokri, N. Investigation of foam flow in a 3D printed porous medium in the presence of oil. *J. Colloid Interface Sci.* **2017**, *490*, 850–858, doi:10.1016/j.jcis.2016.12.015.
76. Chan, H. N.; Chen, Y.; Shu, Y.; Chen, Y.; Tian, Q.; Wu, H. Direct, one-step molding of 3D-printed structures for convenient fabrication of truly 3D PDMS microfluidic chips. *Microfluid. Nanofluidics* **2015**, *19*, 9–18, doi:10.1007/s10404-014-1542-4.